

# Conditions for self-assembly of quantum fortresses and analysis of their possible use as quantum cellular automata

T. E. Vandervelde and R. M. Kalas

*Department of Physics, University of Virginia, Charlottesville, Virginia 22904*

P. Kumar, T. Kobayashi, T. L. Pernell, and J. C. Bean<sup>a)</sup>

*Department of Electrical and Computer Engineering, University of Virginia, Charlottesville, Virginia 22904*

(Received 19 August 2004; accepted 10 November 2004; published online 24 January 2005)

In this study, we detail the conditions that result in the generation of self-assembled quantum fortresses (QFs), in SiGe/Si. A QF consists of four quantum dots (QDs) clustered around a central square pit, one QD per side. This structure strongly resembles the proposed quantum cellular automata (QCA) unit cell—the basis for a computer architecture. We map the growth conditions (epilayer thickness and Ge concentration) under which self-assembly of strain-stabilized QFs and their precursors occur. Additionally, we characterize how QFs change in height, width, and internal size scales within this parameter space. From this information, we develop a phenomenological model for why QFs form based upon changes in lattice spacing. We then calculate how QFs of the observed shapes and sizes would function as QCAs based on a Hubbard-type Hamiltonian model. This analysis reveals that self-assembled QFs grown at 550 °C, a rate of 1 Å/s, a SiGe alloy composition of 37–40%, and a thickness of 15–35 nm could be used as QCAs. © 2005 American Institute of Physics. [DOI: 10.1063/1.1844620]

## I. INTRODUCTION

Over the past century several forms of epitaxial growth have been documented.<sup>1</sup> At one extreme, planar, atomic, layer-by-layer growth occurs when the interfacial energy is small. This mode, called Frank–van der Merwe (FM) growth, usually arises when epitaxial layers have nearly the same lattice constant as the substrate.<sup>2</sup> At the other extreme, epitaxial material may immediately cluster into three-dimensional (3D) islands. This mode, called Volmer–Webber (VW) growth, occurs when interfacial energies are high, a condition that arises when epi and substrate materials have radically different lattice constants.<sup>3</sup> Between these two extremes is Stranski–Krastanov (SK) growth, which involves the initial smooth growth of atomic layers, as seen in FM growth, followed by a transition to a 3D topology similar to VW growth.<sup>4</sup> This transition occurs once the epi strain energy exceeds a critical cumulative level.

In the last 15 years, an appreciation of SK islanding has evolved from that of an undesirable side effect to the object of intense study. Indeed, SK growth is now proposed as the solution for a range of scientific and technological challenges. For example, many of the new device architectures being explored use SK growth.

SiGe on Si is a prototypical SK system. After the growth of an initial wetting layer, the epilayer undergoes a two-dimensional (2D) to 3D transition. The reduction in energy via strain relief exceeds the increase in surface energy due to the increased surface area.<sup>5</sup> This topological shift is due to the 4.2% difference in the lattice parameter between Si and Ge, which generates a large amount of strain at the interface.

The areal elastic strain energy in the epilayer can be expressed via a continuum elasticity theory as  $E_{el} = 2G\varepsilon_0^2(1 + \nu)h/(1 - \nu)$ ,<sup>6</sup> where  $\nu$  is the Poisson ratio of the epilayer,  $G$  is the epilayer shear modulus,  $h$  is the epilayer thickness, and  $\varepsilon_0$  is the epilayer strain. The epilayer strain is calculated using the lattice parameters of the two materials,

$$\varepsilon_0 = \frac{a_e - a_s}{a_s}.$$

This indicates that tetragonally distorted epitaxial layers store elastic strain energy on the order of  $2 \times 10^7 \text{ J m}^{-3}$ , for a lattice mismatch of 0.01. For these levels of energy, the transition to a 3D growth mode, or introduction of some other strain relief mechanisms, is very likely. In fact, two competing mechanisms attempt to relieve this strain: dislocations and islanding. Strain relief by dislocations dominates when the strain is large, while islanding occurs for a low strain.

For SK growth, initial strain-relieving topology generally takes the form of either pits or small pyramidal islands, called hut clusters.<sup>5,7,8</sup> These structures share several features—both are pyramidal in shape, tend to form {105} facets, and are aligned along the [100] direction.<sup>7</sup> For hut clusters to continue growing, new atomic layers must first overcome an energetic nucleation barrier. Eventually, the barrier to form larger {105} facets becomes too great and the hut clusters evolve morphologically, changing into domelike structures.<sup>9</sup>

Domes have a series of smaller planes, primarily {201} and {311}, and a more spherical shape. These domes grow by absorbing material from the surrounding structures until they plateau; beyond this point, they must dislocate to continue growth. At greater epilayer thicknesses, this structure fails to relieve the ever-increasing amount of strain energy, causing

<sup>a)</sup>Electronic mail: jcb6t@virginia.edu

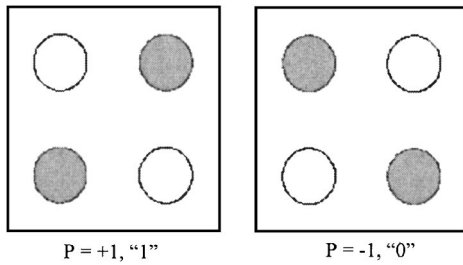


FIG. 1. The basic QCA unit cell—the two possible antipodal configurations of electrons on the four quantum dot unit cell. The polarizations of +1 and -1 can represent the binary states “0” and “1,” respectively.

dislocations to emerge as the dominant form of strain relief. The resultant islanding becomes less organized and pronounced.

The above work on island structures has been paralleled by studies on their physical properties. Scientists have studied how shrinking a structure’s dimensions affects the electrical properties of semiconductors. Dimensions below the de Broglie wavelength of the electron (or hole) result in quantum confinement of the charge carrier in that dimension. Analysis of such structures has evolved in a natural progression of low-dimensional structure studies: quantum wells, a quasi-two-dimensional system in the 1970s,<sup>10,11</sup> quantum wires, a quasi-one-dimensional system in the 1980s;<sup>12</sup> and Quantum dots (QDs), a quasi-zero-dimensional system in the 1980s and 1990s.<sup>13,14</sup> Due to their physical confinement in three dimensions, QDs can be viewed as atomlike and are often referred to as artificial atoms. Theoretical studies of these structures are quite advanced. Indeed, in many cases, the mathematical techniques needed to analyze QDs were discovered long before the structures themselves were first created.<sup>15</sup>

For those working in the field of computer engineering, a particularly exciting possible use for QDs is that of quantum cellular automata (QCA) architectures. The Lent collaboration at the University of Notre Dame suggest this use of QDs.<sup>16–25</sup> The arrangement of four QDs in a square structure (Fig. 1) can be used to replace switching transistor latches, generating a basis for computer architecture. If interdot barriers are high enough, electrostatic forces will drive the charges into antipodal positions within the cell and electrons localize to individual dots. This results in a bistable state, with polarizations of  $P=+1$  and  $P=-1$ , which can be equated to the digital logic equivalent of binary “0” and “1.” These bistable individual cells can then be combined to replicate all of digital logic.

To date, QCA (and most QD-based structures) have been fabricated using high-resolution processing techniques such as electron-beam lithography. While these have produced intriguing demonstrations, they are ultimately impractical. Beam lithography uses a sequential point-by-point writing that steers the beam across the area to be patterned. While scanning velocities can be quite large, one is ultimately limited by the need to linger long enough to expose a resist material or etch or deposit sufficient material to define a pattern. These time constraints mean that conventional wafers would require patterning times measured in hours, ren-

dering such processes economically unacceptable. Spontaneous self-assembled structures could solve this problem. A promising example of self-assembly is included in the work of Deng and Krishnamurthy, who identified growth conditions that produce a tight square clustering of four islands. These structures, described as “quantum molecules,”<sup>26</sup> bear a striking resemblance to the four QD patterns called for in QCA designs. Deng and Krishnamurthy’s work used a predeposition of 1/5th monolayer (ML) of carbon to nucleate pits. These pits would then act as nucleation sites for islands at their edges. In this work, we focus on a similar, naturally forming structure called a quantum fortress (QF).<sup>27,28</sup> A QF consists of four QDs aligned along the sides of a square pit, where in some cases the islands have elongated to the point of forming a continuous square wall. For this structure, neither pre patterning nor carbon predeposition is required. The quadra-axial pattern of QFs suggests the use of self-assembly to generate semiconductor-based QD-QCAs.

Experimental techniques are described in Sec. II. The physical dimensions and relationship between surface morphologies and growth conditions are explored in Sec. III. This includes a mapping of the parameter space under which QFs form, statistics on how QFs evolve in height and width as a function of strain energy, a lattice parameter-based model of why QFs form, and a discussion of some of the more unusual structures seen for certain growth conditions. The analysis of these results and interpretation of the possible utility of QFs for QCA purposes are discussed in Sec. IV.

## II. EXPERIMENT

In this work,  $\text{Ge}_x\text{Si}_{1-x}$  films were grown via molecular-beam epitaxy (MBE) on (001)Si substrates. The experiments were carried out using a custom-built VG 90S double-chamber UHV-MBE system at the University of Virginia (UVA).<sup>29</sup> Before sample growth, a modified “piranha clean” procedure<sup>30</sup> was employed to clean and hydrogen-passivate the substrates. The resulting hydrogen-terminated layer, along with any surface oxide, was desorbed within the MBE system, at a temperature of 775 °C. A 1000-Å Si buffer layer was then grown at a starting temperature of 775 °C. The substrate temperature was gradually lowered to a SiGe growth temperature of 550 °C during deposition of the epilayer. This procedure allows for immediate growth of the epilayer, thereby eliminating any chance of contamination buildup. The base pressure in the chamber prior to growth was typically  $2 \times 10^{-10}$  Torr.

Standard growth procedures for our MBE system include rotating the sample to eliminate gradients in composition and epilayer thickness over the wafer. However, in order to use the system to its full potential, we chose to utilize a combinatorial epitaxy technique by not rotating most samples. Without rotation, we effectively add both a thickness and a compositional gradient across the surface of the wafer. ( $\Delta_{\text{thick}}=15\%$  and  $\Delta_{\text{comp}}$  up to 50%) (Fig. 2). The gradients are due to the physical separation of the evaporation sources, relative to each other and the sample (Fig. 3). From the cosine law of emission and the properties of sources, we

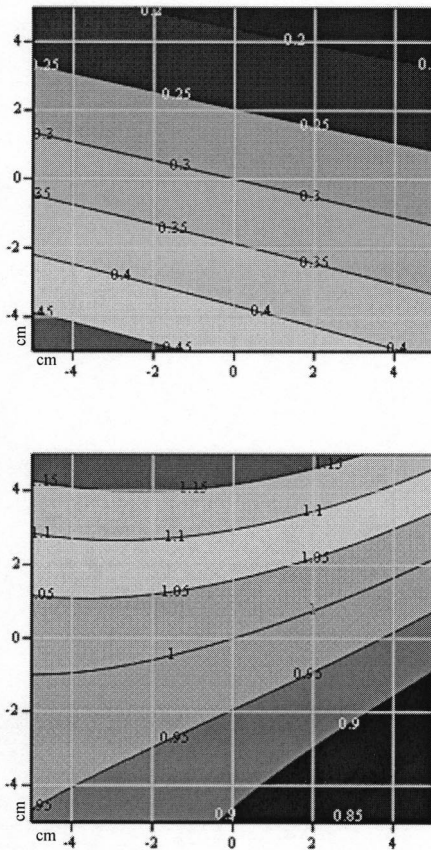


FIG. 2. Compositional map (upper) and thickness map (lower) for a center  $10 \times 10$  cm region of a nonrotated 200-mm wafer; by using the cosine law of emission, we calculate the epilayer germanium fraction and relative thickness vs position on the wafer. Both plots assume a central germanium fraction of 30%.

calculated the thickness and Ge fraction at any point of the wafer.<sup>31</sup> These calculations were checked against calibration samples, yielding a maximum discrepancy of 10% (e.g., for a Ge composition of 10%, the measured value would be between 9% and 11%).

Growth results were characterized through the use of

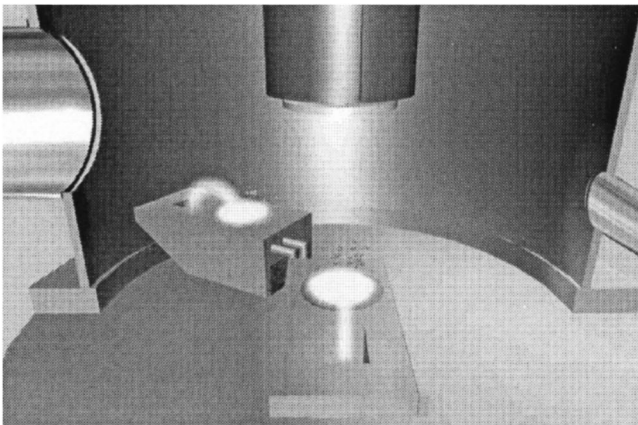


FIG. 3. Spatial configuration of the Si and Ge evaporation sources; Si source in the foreground, Ge at the back right, wafer facing downward from above.

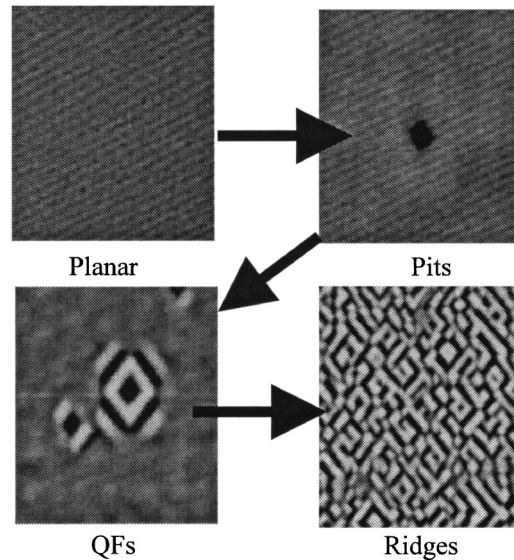


FIG. 4. Morphological evolution as observed by AFM. As growth progresses, the structures go through four stages of evolution. First the adatoms attach to form the wetting layer. Then, as the strain increases, planar growth transitions to a 3D topology (i.e., square pits appear). Next, incoming adatoms attach along the sides of the pits due to additional material and strain, thus forming QFs. Finally, continued deposition results in a morphological transition into a series of ridges at  $90^\circ$  to each other (note that this is sometimes accompanied by dislocation formation).

*ex situ* tapping mode atomic force microscopy (AFM). This microscopy was done using a Digital Instruments' Dimension 3100 Nanoscope AFM.

### III. RESULTS

#### A. QF growth results

The initial focus of this work was to characterize the conditions under which QFs form. QFs have been shown to be part of an evolutionary series of surface morphologies, much like hut clusters and domes.<sup>27,28</sup> Figure 4 shows the typical surface feature evolution as SiGe is deposited. We first see only planar growth and, occasionally, a small amount of rippling, which gives way to pits. These strain-relieved regions occur along the lateral sides of a pit and collect adatoms, causing islands to form at their borders. Continued deposition results in classical ridgelike structures covering the surface and eventual relaxing of the epilayer via dislocations.

To understand this process, we explored the different surface morphologies (i.e., pits, QFs, and ridges) as a function of growth conditions. In our earliest studies, we employed a 30% Ge alloy with a thickness of 5–200 nm over 15 samples. These experiments were subsequently repeated using base Ge concentrations of 20% and 40%, and thickness ranges of 75–350 nm and 5–40 nm, respectively. Additionally, the effects of growth temperature, between 400 and 750 °C, under known QF-generating conditions (30% Ge and a 50-nm epilayer) were also explored.

On a single wafer, the thickness and composition each occur in a gradient, by a combinatorial epitaxy technique, which allows for simultaneous examination of multiple conditions. This technique allows for all of the above morpholo-

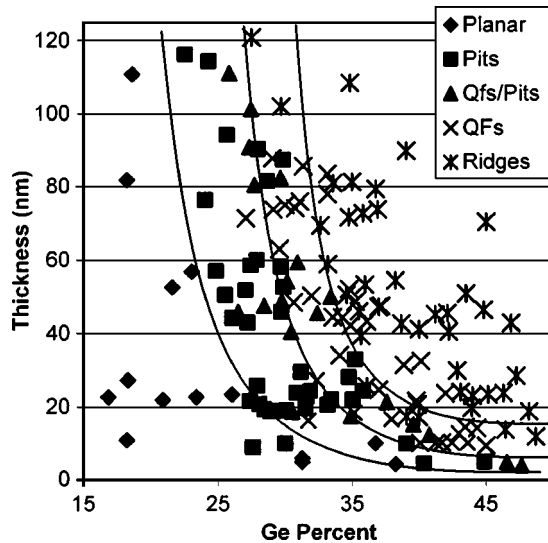


FIG. 5. Structures observed vs Ge fraction and epilayer thickness. Plot of data points for growth conditions vs morphology. As strain energy increases, either by increasing Ge percentage or epilayer thickness, morphology shifts from planar growth, to pits, to QFs, to ridges. (Note that stated epilayer “thickness” is the thickness the layer would have if growth had occurred in a smooth planar manner.)

gies to be observed on a single wafer. The most powerful aspect of this technique is that it allows us to examine, in great detail, the transition(s) between morphologies.

For our experiments, each scanned point on the wafer was subsequently analyzed for Ge percentage and epilayer thickness using the compositional mapping equations discussed above. Compilation of the data allowed for comprehensive mapping of surface morphology as a function of growth parameters (Fig. 5). We found conditions defining the boundaries of the different surface features to follow exponential-like decay lines. As samples become more Ge rich, the thickness required to generate pits and other features decreases. This continues until the formation of these structures is no longer favorable, giving way to hut clusters at around 50% Ge. As shown in Fig. 5, the complete range of morphologies can occur at a single thickness. Pits are observed when Ge concentration is low, and ridges when it is high. Similarly, a variation in thickness at constant Ge concentration induces morphological changes, from planar through ridges. Interestingly, QFs occur under highly varied growth conditions—forming over a thickness range of nearly two orders of magnitude and a factor of 5 for Ge concentration. For QFs to be produced when one growth parameter is fixed, however, all the other parameters are effectively limited to a small range.

While the basic structure of QFs remains constant, increasing thickness causes the length of the lateral walls to increase until adjacent walls meet (Fig. 6). Conversely, as Ge concentration increases and epilayer thickness decreases, the lateral length of QFs decreases. This behavior, which agrees with standard observations of strain-stabilized islanding, has functional implications that will be discussed in more detail in the analysis section of this paper.

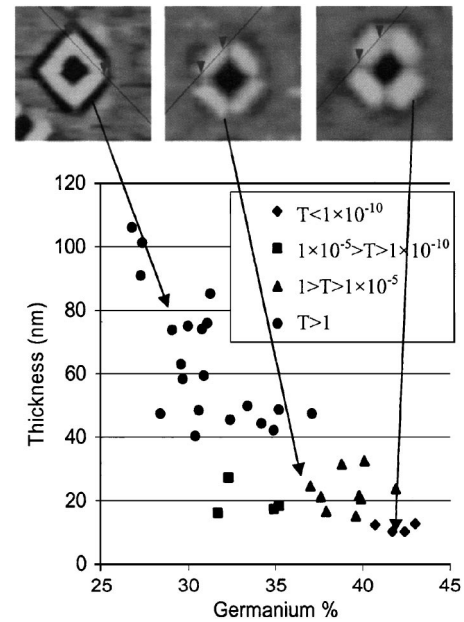


FIG. 6. Alternate QF structures. AFM images of QFs grown with different combinations of thickness and Ge fraction. QFs that were formed under thick epilayer conditions are larger and have little or no gaps between the islands, whereas those formed with a high Ge fraction are usually less than half as large with wide gaps between the islands.

Under certain growth conditions, we observed more complex structures than those described above. For instance, certain QFs develop a moatlike trench that surrounds their islands and additional sets of islands beyond. We call these structures double-wall QFs (DW-QFs) (Fig. 7). At first it was not obvious whether these additional walls occur due to interactions with surrounding QFs or if they arise as a natural byproduct of the QF growth process. The appearance of DW-QFs in regions more sparsely populated with QFs suggests that this process does not require interactions with neighbors. In addition, we see formations we have termed “quantum antiwires” or “slits” (Fig. 7). The slits are elongated pits in the  $\{100\}$  and  $\{010\}$ , sometimes turning at  $90^\circ$  angles. Slits were only observed in samples with a thin epilayer ( $\sim 5$  nm) and in slightly thicker samples ( $\sim 10$  nm) that were purposely annealed.

## B. QF characterization

To develop a better understanding of the mechanics of QF formation, structures were cross sectioned using tapping mode AFM. (Fig. 8). Cross sectional analysis was performed using software provided with the AFM (Fig. 9). Widths were measured by summing the two peak-to-trough measurements, effectively giving a peak-to-peak measurement of the QF size. This technique was employed for two reasons. First, it allowed for simultaneous measurement of the QF’s trough-to-peak height and facet angle. Second, it eliminated a subjective evaluation of base line height. As shown in Fig. 9, as elastic strain energy increases, the width and height also increase. Each point on the graph indicates the mean value of the dimension in question for all the QFs in a  $5 \times 5 \mu\text{m}$  scan area. If saturation of QF size occurred, observed changes would be the result of a maturation process. To address this

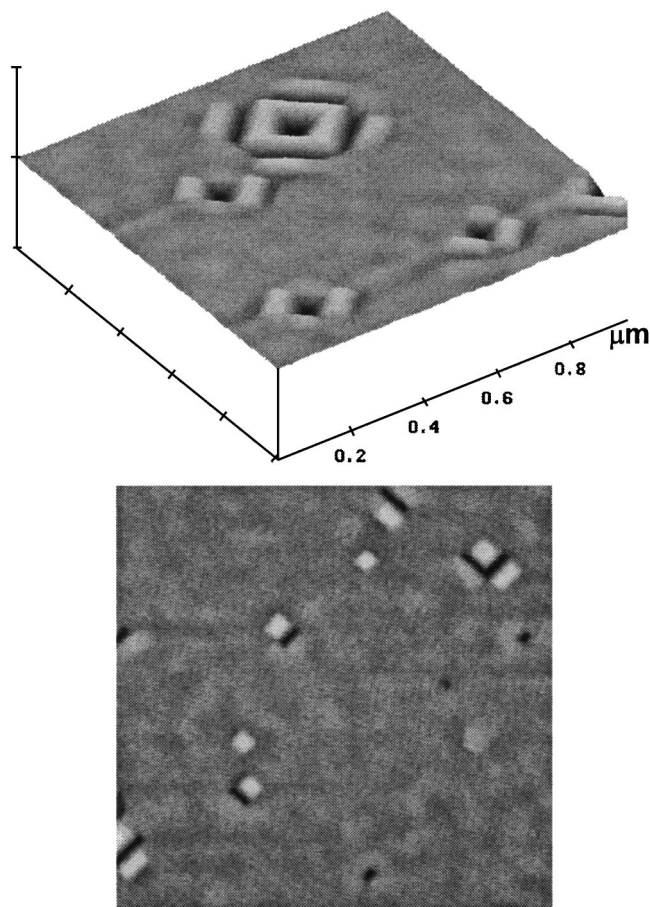


FIG. 7. Double-walled QFs and antiwires: (a) QFs surrounded by a moatlike trench and an extra ring of islands. (b) An example of elongated pits, also called 'quantum anti-wires' or 'slits.' These structures form in thin samples with an epilayer thickness less than 10 nm if an anneal is performed after growth.

issue, we also plotted the maximum size for a QF in each scan. As the plots indicate, QF height and width tend to increase with strain energy without any direct evidence of saturation.

The formation of QFs can be explained through a phenomenological model of lattice expansion and preferential deposition via segregation. Recall here that we are depositing a larger lattice-constant material on a smaller lattice-constant substrate without dislocations. After the growth of an initial wetting layer, strain builds up in the deposited material until pits form [Fig. 10(a)]. Once pits begin to grow, the lattice near their edges relaxes through expansion [Fig. 10(b)]. In-

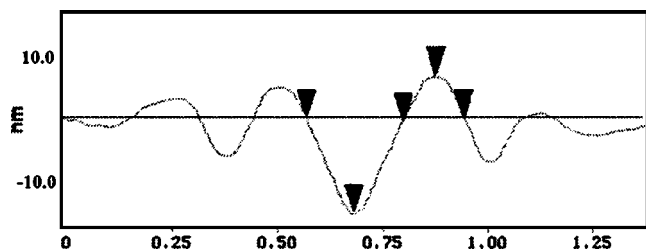


FIG. 8. Typical AFM cross section of a QF. The placement of cursors indicates where the peak-to-peak width and peak-to-trough height were evaluated.

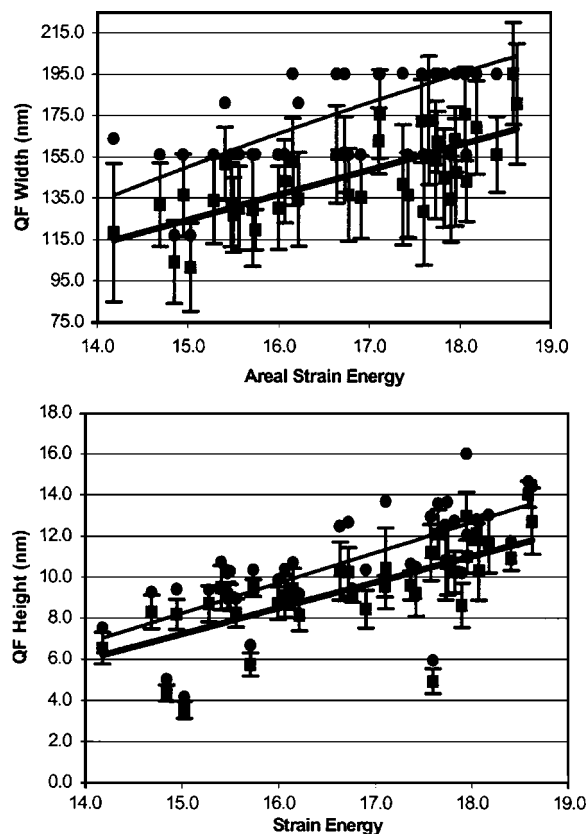


FIG. 9. QF height and width increase with strain energy. (Upper panel) peak-to-peak width of QFs increase as a function of uncompensated strain energy. (Lower panel) trough-to-peak height increase as a function of uncompensated strain energy. The diamonds represent the average of all QFs in a  $5 \times 5 \mu\text{m}$  scan area; the squares represent the maximum from each scan.

cident adatoms preferentially deposit near the edges of the pits due to this local lattice relaxation. Similarly, adatoms are repelled by lattice contraction near the bottoms of the pits. This process slowly deepens the pits until they form energetically stable  $\{105\}$  facets. With continued deposition, preferential attachment of adatoms at the relaxed areas, outside the pits, eventually leads to island formation [Fig. 10(c)]. Beneath the islands, the lattice is expanded, which produces compression in adjacent regions. Lattice compression on the far side of the islands discourages local attachment [Fig. 10(d)]. Some QFs stop evolving at this point due to a lack of material and/or strain energy. These QFs often have only a shallow moat surrounding them, similar to the depression rings seen around the domes. In many cases, however, this process progresses to form DW-QFs; the moat continues to develop, allowing the surrounding lattice to relax in the same manner as the original pit. This relaxation results in the appearance of a new zone of preferential adatom attachment, leading to the formation of outer islands [Fig. 10(e)]. These outer islands could potentially be used as platforms for applying a gate voltage to the inner islands or as an external clocking mechanism.

If the growth is terminated just after pit formation and the sample is annealed, we may see the appearance of slit structures, though less commonly than QFs. The  $\{105\}$ -faceted pits expand in the  $\langle 010 \rangle$  directions, forming elon-

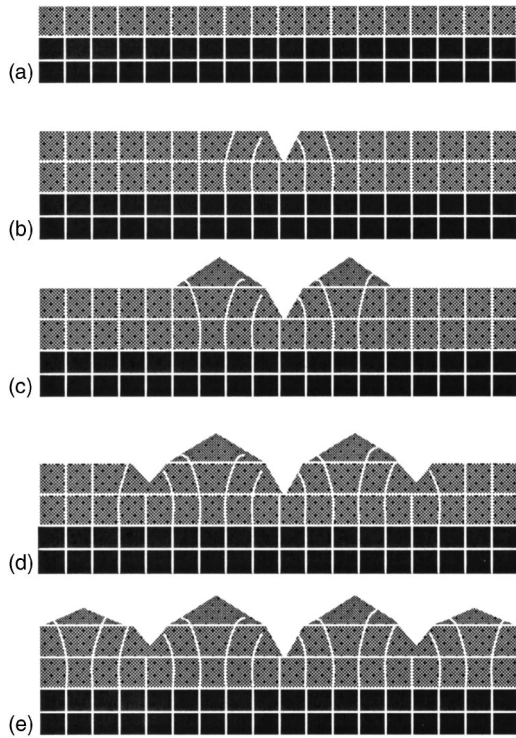


FIG. 10. Model of QF formation based on lattice dilation and compression. (a) A uniformly compressed epilayer on Si. (b) Formation of pits allows dilation of the adjacent lattice, relieving strain locally. (c) The area of relieved strain attracts adatoms, leading to island formation along the edges of the pits. (d) Further growth of islands compresses the lattice near their edges, discouraging adatom attachment and forming a trench along their border. (e) Trench formation allows for additional lattice expansion and strain relaxation. This strain relief then nucleates a second ring of islands outside the structure, forming a double-walled QF.

gated slits to relieve additional strain along its borders. These slit structures only form for thin epilayers of less than 10 nm.

#### IV. ANALYSIS

In order to gain insight into the suitability of self-assembled QFs for QCA circuits, we examined the quantum-mechanical switching of a unit cell. In the following analysis, the intradot degrees of freedom and forms of dissipative coupling are ignored. These factors do not play a major role in the two-cell system we analyzed. Figure 1 depicts the basic unit cell employed for our calculations.

Using the technique developed by Lent and Tougaw, we began with the Hubbard-type Hamiltonian for a QCA unit cell,<sup>18</sup>

$$H_0^{\text{cell}} = \sum_{i,\sigma} E_0 n_{i,\sigma} + \sum_{i>j,\sigma} t_{i,j} (a_{i,\sigma}^\dagger a_{j,\sigma} + a_{j,\sigma}^\dagger a_{i,\sigma}) + \sum_i E_Q n_{i,\uparrow} n_{i,\downarrow} + \sum_{i>j,\sigma,\sigma'} V_Q \frac{n_{i,\sigma} n_{j,\sigma'}}{|\mathbf{R}_i - \mathbf{R}_j|},$$

where the first term represents the on-site energy for each dot and  $n_{i,\sigma}$  represents the number operator for a particle on site  $i$  ( $i=1,2,3,4$ ) with spin  $\sigma$ . The second term accounts for the total cost of two particles tunneling within sites  $i$  and  $j$ , where the coupling energy,  $t_{ij}$ , is the energy associated with this tunneling, and  $a_{i,\sigma}$  is a standard annihilation ladder op-

erator for the destruction of a particle at site  $i$  with spin  $\sigma$ . The third term denotes the Coulombic cost of placing two electrons, with opposite spins, on one site. The fourth sum represents the Coulombic potential due to electrons at positions  $\mathbf{R}_i$  and  $\mathbf{R}_j$  on the  $i$ th and  $j$ th sites. Since it represents the lowest-energy state, we chose to examine the case where the electrons' spins are antiparallel. Additionally, to keep charge neutrality in each cell, we used a fixed positive charge,  $\rho^f = (1/2)e$ , at each site. Although for a single cell this neutralizing charge simply renormalizes  $E_0$ , it becomes increasingly important as the number of interacting cells increase. Should each cell have a negative charge, the electrons would respond more to the net charge from the other cells than the net polarization.

To examine the cell's polarization-switching ability, we must consider the interactions between neighboring cells and the electrostatic environment. We solve the time-independent Schrödinger equation to understand these interactions with a second Hamiltonian term,  $H_{\text{neighbor}}^{\text{cell}}$

$$(H_0^{\text{cell}} + H_{\text{neighbor}}^{\text{cell}})|\Psi_n\rangle = E_n|\Psi_n\rangle.$$

The total Hamiltonian can then be diagonalized directly into the basis for a two-particle ket. The single-particle density,  $\rho_i$ , is calculated from the two-particle ground-state wave function,  $|\Psi_0\rangle$ , by finding the expectation value of  $n_{i,\sigma}$

$$\rho_i = \sum_{\sigma} \langle \Psi_0 | n_{i,\sigma} | \Psi_0 \rangle.$$

These densities can then be used to calculate polarization,  $P$ , using

$$P \equiv \frac{(\rho_1 + \rho_3) - (\rho_2 + \rho_4)}{\rho_1 + \rho_2 + \rho_3 + \rho_4},$$

where  $\rho_i$  represents the electron probability density at site  $i$ . Electrons completely localized to sites 1 and 3 will yield a polarization of  $P=1$ , while localization to sites 2 and 4 yield  $P=-1$ .

For the use of QFs as QCA, the polarization of the neighboring cells must influence the state of a cell in a strongly nonlinear fashion. To this end, we calculated the response of one QF (cell<sub>1</sub>) to another QF (cell<sub>2</sub>), where cell<sub>2</sub> is at a fixed polarization and the centers of the cells are separated by three times the characteristic cell width,  $3a$ , or approximately 300 nm. For this model, we assume that cell<sub>2</sub> has a polarization,  $P_2$ , which we can control. Here, the additional electrostatic potential at each site in cell<sub>1</sub> due to the corresponding electron density on each site in cell<sub>2</sub> is included in the Hamiltonian for cell<sub>1</sub>. This yields a perturbing component in the Hamiltonian of the form

$$H_{\text{neighbor}}^{\text{cell}} = H_1^{\text{cell}} = \sum_{i \in \text{cell}1,\sigma} V_i^1 n_{i,\sigma},$$

where

$$V_i^m = \sum_{k \neq m,j} V_Q \frac{(\rho_j^k - \rho^f)}{|\mathbf{R}_{k,j} - \mathbf{R}_{m,i}|}$$

is the potential due to the charges on site  $i$  in cell  $m$ . The electron density at site  $j$  in cell  $k$  is  $\rho_j^k$ ; the position of site  $j$

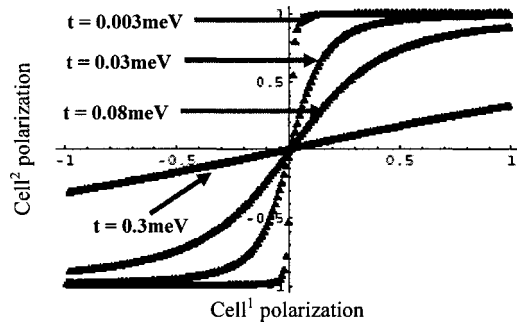


FIG. 11. Calculated cell-cell response for a QCA-based structure with QF-like properties. For small values of  $t$ , we see a very nonlinear transition in the polarization of  $P_1$  as the polarization of  $P_2$  is switched from  $-1$  to  $1$ . As the value of  $t$  increases, however, the nonlinearity of the switching breaks down.

in cell  $k$  is  $\mathbf{R}_{kj}$ . Thus, the total Hamiltonian for cell<sub>1</sub> is

$$H^{\text{cell}} = H_0^{\text{cell}} + H_1^{\text{cell}}.$$

Using this Hamiltonian, we can solve the two-electron time-independent Schrödinger equation for the ground-state polarization of cell<sub>1</sub>,  $P_1$ , for a series of  $P_2$  values in the range  $[-1, 1]$ . This analysis yields the induced polarization of cell<sub>1</sub> due to cell<sub>2</sub>,  $P_1(P_2)$ , the cell-cell response function. We expect to see a nonlinear response, such as shown in Fig. 11. This function offers us a predictor of QCA performance.

Before we can calculate the functionality of QFs as QCA, we must first define the parameters within the Hamiltonian. Based on our experimental data for QFs, we can make reasonable approximations for each parameter.  $E_0$  can be estimated as the depth of the quantum well defined by the island. A typical QF island of  $50 \times 200 \text{ nm}^2$  yields  $E_0 = 150 \text{ meV}$ .  $V_Q$  is calculated by using the dielectric constant for the  $\text{Si}_{1-x}\text{Ge}_x$  alloy. For simplicity, we assume a Ge concentration of  $x=0.3$ . We employed the same approximation as Lent and Tougaw, and defined  $E_Q = V_Q / (D/3)$ , where  $D$  is the length of the island.<sup>18</sup> The value for the coupling energy,  $t_{ij}$ , is calculated using the separation between the islands, the island size, and the tunneling barrier determined from the wetting-layer properties. Therefore, we calculated  $t_{ij}$  by using a double-well model and WKB approximation (Fig. 12).<sup>32,33</sup> To do this, we first calculated the tunneling probability, starting with

$$\gamma = \frac{1}{\hbar} \int_0^a dx \sqrt{2m(V_0 - E)} = \frac{a}{\hbar} \sqrt{2m(V_0 - E)},$$

the tunneling probability is

$$T = e^{-2\gamma} = e^{-2a/\hbar \sqrt{2m(V_0 - E)}}.$$

Thus, we can now calculate the tunneling frequency,

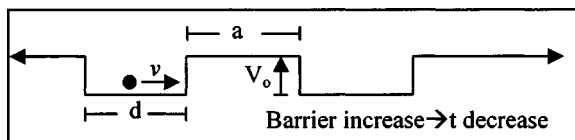


FIG. 12. Schematic of a basic double well, where  $d$  is the width of each well and  $a$  is the separation between the wells.

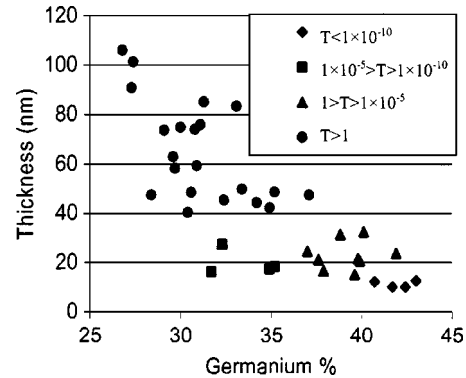


FIG. 13. Approximate values of QCA coupling energy (in meVs) for QFs grown at various thicknesses and Ge fractions. Coupling energies indicated by the symbols. Here, large values of  $t$  equate to QFs with large islands and small or nonexistent gaps between them and small values of  $t$  equate to small islands with large gaps between them. For values of  $t$  between 0.00001 and 1 there is some hope for functionality. We call this region the “Goldilocks” region.

$$\omega = \frac{v}{2d} e^{-2\gamma},$$

and the coupling energy,

$$t = \omega \hbar = \frac{\hbar v}{2d} e^{-2a/\hbar \sqrt{2m(V_0 - E)}}.$$

Two things are critical in analyzing how an island’s size and the interisland gaps affect tunneling. First, if interdot barriers are too low,  $t$  is high, and the electrons will not localize well. Second, if the barriers are too high,  $t$  is too low and the switching times,  $T_{\text{switch}}$ , become too long, as

$$T_{\text{switch}} = \frac{\hbar}{t}.$$

The most promising QF-based QCA candidates would have a median value of  $t$  ( $\sim 10^{-3} \text{ meV}$ ). This “Goldilocks” region, which is depicted in Fig. 13, has a Ge composition of 37%–40% and an epilayer thickness of 15–35 nm. Figure 14(a) illustrates our calculated cell-cell response function for QF-based QCA from this region and demonstrates the classic bistable saturation that is the basis of QCA architectures. This sharp nonlinearity is crucial because it allows us to assign binary logic numerals to our polarization states: 1 to the  $P=+1$  state and 0 to the  $P=-1$  state. Figure 14(b) shows the four lowest eigenenergies for cell<sub>1</sub> as a function of cell<sub>2</sub>’s polarization. As indicated, any perturbation of cell<sub>2</sub>’s polarization quickly breaks the degeneracy in cell<sub>1</sub>’s polarization state. The energy-level spacing for a fully polarized state, corresponding to 0.15 meV, indicates the temperature at which the cell can flip to a higher-energy state, about 1.2 K. As shown in Fig. 14(c), QFs outside this region have problems with the linearity of their cell-cell response, which imply half-states in the cell’s polarization.

## V. CONCLUSIONS

We have systematically explored the parameter space under which QFs and their morphological cousins appear. We showed that these strain-induced features are generated

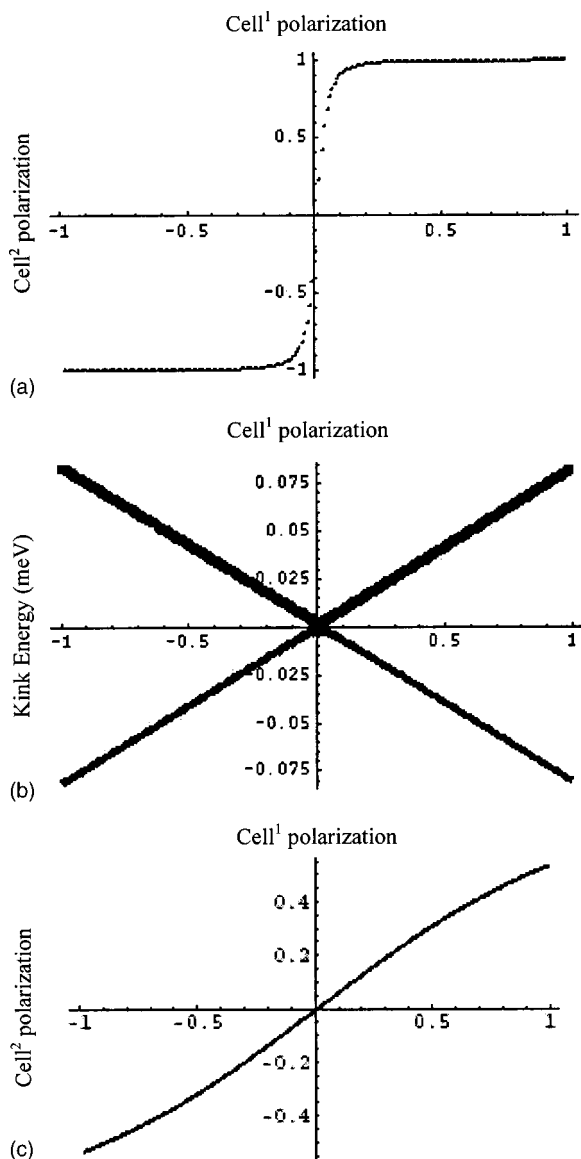


FIG. 14. Phase and energy plots of QFs as QCA. (a) Nonlinear steplike switching of a QF-based cell from the “Goldilocks” region of Fig. 13. (b) Plots of the four lowest eigenstates for QFs. The difference between the lines indicates the energy it would take to antialign the two cells as a function of the driver cell’s polarization. (c) For cell–cell responses of QFs outside of the Goldilocks region, nonlinearity breaks down. This generates mixed states and prevents the cell from functioning as desired.

under a wide range of growth conditions, limited to a narrow band of interdependent parameters. We also observed that as the areal-strain energy driving these structures increases, their height and width also increase. This variance could have important technological implications, allowing for selection of QF dimensions. The natural fourfold symmetry of these structures strongly suggests their use in QCA-based architectures. This is borne out by our calculations.

QFs show great promise for use in QCA-based architectures; they still lack control of position, however. Using natural unguided growth mechanisms, we cannot achieve the complex architectures that a QCA-based circuit would require. Thus, we need a mechanism with which to guide the nucleation points of these structures. Our group is currently researching a way to expand the technique and guide QF

nucleation. Our QFs lack an additional QCA feature, cells rotated by  $45^\circ$ . For instance, these rotated cells are used in the QCA-based adder. While self-assembly may not provide such rotated cells, a slightly modified version, using spacing offsets, is just as effective at yielding these logic elements without the need for rotated cells.<sup>18</sup>

Finally, our quantum-mechanical analysis of QF charge energies determined that they could serve as QCAs, but only at temperatures  $\leq 1.2$  K. This limitation, however, could be overcome by changing the manner in which QFs are grown. If the pit size was reduced, then the overall size of the QF was smaller, and operational temperature climbed, increasing their utility. One might accomplish this through predeposition of a surfactant, such as gallium or antimony.

In conclusion, through this study, we have characterized the growth conditions under which QFs form. We saw that QFs arise under a wide range of interdependent growth conditions. QFs were shown to grow in both width and height as a function of epilayer strain energy. More complex structures, including double-walled QFs and elongated slits, were also observed. The formation of all of these structures was explained through a simple strain-based model. This model describes the effect of lattice contractions or relaxations on adatom attachment, which would drive the pit or island growth, respectively. Since QFs have the same quadra-axial pattern as prescribed for a QCA unit cell, we employed a Hubbard-type Hamiltonian model to check their possible function as QCA. Analysis of the physical parameters of QFs revealed that some, indeed, could function as QCAs. The operational temperatures of these QFs, however, would be limited to cryogenic helium temperatures.

## ACKNOWLEDGMENTS

The authors would like to thank Audrey Eisen-Vandervelde, Adam Phillips, Andrea Soddu, Eugene Kolomeisky, Jennifer Gray, Surajit Atha, and Robert Hull for helpful discussions. This work was partially funded by NSF-DMR through the NSF-MRSEC at UVA, “The Center for Nanoscopic Materials Design” and the UVA-UIUC-IBM-Sandia Focused Research Group “Nanoscale Morphological Evolution of Semiconductor Surfaces” (Grant No. 0075116).

<sup>1</sup>J. A. Venables, *Thin Films: Heteroepitaxial Systems* (World Scientific, Singapore, 1998), Chap. 1.

<sup>2</sup>F. C. Frank and J. H. van der Merwe, *Proc. R. Soc. London, Ser. A* **198**, 205 (1949).

<sup>3</sup>M. Volmer and A. Weber, *Z. Phys. Chem., Stoechiom. Verwandtschaftsfl.* **119**, 277 (1926).

<sup>4</sup>I. N. Stranski and L. Krastanow, *Sitzungsber. Akad. Wiss. Wien, Math.-Naturwiss. Kl., Abt. 2B* **146**, 797 (1938).

<sup>5</sup>D. E. Jesson, K. M. Chen, S. J. Pennycook, T. Thundat, and R. J. War-mack, *Phys. Rev. Lett.* **77**, 1330 (1996).

<sup>6</sup>R. Hull and J. C. Bean, *Semicond. Semimetals* **56**, 102 (1999).

<sup>7</sup>Y. W. Mo, D. E. Savage, B. S. Swartzentruber, and M. G. Lagally, *Phys. Rev. Lett.* **65**, 1020 (1990).

<sup>8</sup>J. Tersoff and F. K. LeGoues, *Phys. Rev. Lett.* **72**, 3570 (1994).

<sup>9</sup>M. Tomitori, K. Watanabe, M. Kobayashi, and O. Nishikawa, *Appl. Surf. Sci.* **76/77**, 322 (1994).

<sup>10</sup>L. L. Chang, L. Esaki, and R. Tsu, *Appl. Phys. Lett.* **24**, 593 (1974).

<sup>11</sup>R. Dingle, W. Wiegmann, and C. H. Henry, *Phys. Rev. Lett.* **34**, 1327 (1975).

<sup>12</sup>P. M. Petroff, A. C. Gossard, R. A. Logan, and W. Wiegmann, *Appl. Phys. Lett.* **41**, 635 (1982).

- <sup>13</sup>M. A. Reed, R. T. Bate, K. Bradshaw, W. M. Duncan, W. M. Frensley, J. W. Lee, and H. D. Smith, *J. Vac. Sci. Technol. B* **4**, 358 (1986).
- <sup>14</sup>M. A. Reed, *Sci. Am.* **268**, 118 (1993).
- <sup>15</sup>L. Jacak, P. Hawrylak, and A. Wójs, *Quantum Dots* (Springer, Berlin, 1998).
- <sup>16</sup>C. S. Lent, P. D. Tougaw, and W. Porod, *J. Appl. Phys.* **62**, 714 (1993).
- <sup>17</sup>C. S. Lent, P. D. Tougaw, W. Porod, and G. H. Bernstein, *Nanotechnology* **4**, 49 (1993).
- <sup>18</sup>C. S. Lent and P. D. Tougaw, *J. Appl. Phys.* **74**, 4077 (1993).
- <sup>19</sup>P. D. Tougaw, C. S. Lent, and W. Porod, *J. Appl. Phys.* **74**, 3558 (1993).
- <sup>20</sup>C. S. Lent and P. D. Tougaw, *J. Appl. Phys.* **74**, 6227 (1993).
- <sup>21</sup>P. D. Tougaw and C. S. Lent, *J. Appl. Phys.* **75**, 1818 (1994).
- <sup>22</sup>P. D. Tougaw and C. S. Lent, *Jpn. J. Appl. Phys., Part 1* **34**, 4373 (1994).
- <sup>23</sup>C. S. Lent, P. D. Tougaw, and W. Porod, *PhysComp '94: Proceedings Workshop on Physics and Computation* (IEEE Computer Society, Los Alamitos, 1994).
- <sup>24</sup>C. S. Lent and P. D. Tougaw, *J. Appl. Phys.* **80**, 4722 (1996).
- <sup>25</sup>C. S. Lent and P. D. Tougaw, *Proc. IEEE* **85**, 541 (1997).
- <sup>26</sup>X. Deng and M. Krishnamurthy, *Phys. Rev. Lett.* **81**, 1473 (1998).
- <sup>27</sup>T. E. Vandervelde, P. Kumar, T. Kobayashi, J. L. Gray, T. L. Pernel, J. Floro, R. Hull, and J. C. Bean, *Appl. Phys. Lett.* **83**, 25 (2003).
- <sup>28</sup>J. L. Gray, R. Hull, and J. Floro, *Appl. Phys. Lett.* **81**, 2445 (2002).
- <sup>29</sup>R. Hull and J. C. Bean, *Semicond. Semimetals* **56**, 1 (1999).
- <sup>30</sup>D. A. Glocker and S. I. Shah, *Handbook of Thin Film Process Technology* (Institute of Physics, Philadelphia, 1999), p. E1.0:8.
- <sup>31</sup>L. Maissel and R. Glang, *Handbook of Thin Film Technology* (McGraw-Hill, New York, 1970).
- <sup>32</sup>L. D. Landau and E. M. Lifshitz, *Quantum Mechanics*, 3rd ed. (Pergamon, New York, 1977), p. 50.
- <sup>33</sup>T. E. Vandervelde, S. Atha, T. L. Pernel, R. Hull, and J. C. Bean, *Self-Organized Processes in Semiconductor Heteroepitaxy*, MRS Symposium Proceedings No. 794 (Materials Research Society, Pittsburgh, 2003), p. 111–116.